RSC Advances

PAPER

View Article Online
View Journal | View Issue



Cite this: *RSC Adv.*, 2026, **16**, 12989

# Ultrafast microwave synthesis of Ti-based MXenes with high yields

Jovana Paskaš,[ab] Miloš Dujović,[c] Milica Govedarica,[b] Vasa Radonić,[b] Vladimir V. Srdić[ad] and Nikola Kanas *[be]

We report a microwave-assisted method for synthesizing MXenes that accelerates hydrofluoric acid etching of MAX phases by ~500-fold compared to conventional approaches. $Ti_3C_2$ and $Ti_3CN$ MXenes were obtained from $Ti_3AlC_2$ and $Ti_3AlCN$ within 3 minutes at 220 W, yielding ~90% and 70% product, respectively. The process produces expanded, accordion-like structures that delaminate into flakes with mild ultrasonication, eliminating post-synthesis intercalation. Rapid, uniform heating and hydrogen evolution drive structural expansion and facilitate delamination. Structural and morphological analyses (XRD, XPS, TEM, SEM, DLS, AFM) confirmed their successful synthesis, while electrochemical testing showed performance comparable to conventionally prepared MXenes. This approach establishes a rapid, efficient, and high-yield route for scalable MXene production.

Received 28th December 2025
Accepted 3rd March 2026

DOI: 10.1039/d5ra10068b

rsc.li/rsc-advances



## 1. Introduction

Since their discovery over a decade ago,[1] MXenes have emerged as a versatile and rapidly expanding family of transition metal carbides and nitrides, attracting significant global attention due to their potential applications in many fields.[2,3] These materials are typically described by the chemical formula $M_{n+1}X_nT_z$, where M denotes one or more transition metals, X represents carbon and/or nitrogen, T signifies surface terminations such as –OH, –F, –Cl, *etc.*, and $n$ ranges from 1 to 4.[1,4]

MXenes represent a broad and chemically diverse family of two-dimensional (2D) transition metal carbides, nitrides, and carbonitrides, with over 50 compositions synthesized to date. Their physical and chemical properties can vary significantly depending on composition, surface terminations, and structural characteristics.[5–7] Owing to their high electrical conductivity, large specific surface area, hydrophilicity, efficient electron-transfer capabilities, and tunable surface chemistry, MXenes represent promising platforms for the immobilization of biomolecules such as enzymes, antibodies, and aptamers, making them attractive candidates for biosensing applications.[7] In addition, the precise manipulation and tunability of physicochemical properties, enabled by their abundant surface terminations, facilitate the formation of composite materials, further enhancing their potential in a wide range of other applications,[8–10] including catalysis,[11] energy storage,[12] and electromagnetic shielding.[13,14] In the biomedical domain, MXene nanosheets have been explored for drug delivery applications and show significant promise as efficient sorbents for urea and other uremic toxins.[15,16]

Although MXenes have shown significant potential across a wide range of applications, their synthesis remains a critical bottleneck limiting further development and their broader adoption in various applications. The most commonly employed top-down synthesis approaches rely on selective etching of A element layers (mostly Al) from MAX phases in aqueous solutions of hydrofluoric acid (HF) or mixtures of fluoride salts with hydrochloric acid (HCl).[17–27] These methods face two primary challenges: (i) the process is labor-intensive and time-consuming, involving multiple steps – chemical etching, repeated washing, exfoliation, delamination, collection, and filtration – and (ii) it requires the use of hazardous etchants, including concentrated or chemicals that generate HF *in situ*.[18] To address these limitations, alternative synthesis methods are being developed, including etching parent MAX phases in molten salts such as $CuCl_2$, $SnF_2$, *etc.*, at elevated temperatures.[19,20] Even though this method excludes HF or *in situ* formation of HF, it is a significantly more time- and energy-intensive process and includes etching at elevated temperatures (>600 °C). Additionally, molten salt MXenes are challenging for post-etching exfoliation to single- or a few-layer MXenes and have poor dispersibility in aqueous dispersion due to the hydrophobic nature of mostly Cl-terminated surfaces.[21,22] Most recently, a solvent-free, one-step gas-phase dry etching method was developed using the strong oxidizing power of halogens and hydrogen halide gases – such as $Cl_2$, $Br_2$, $I_2$, HCl, HBr, and HI—to etch various A-elements (*e.g.*, Al, Si, Sn) in MAX phases. As

[a]*University of Novi Sad, Faculty of Technology, Department of Materials Engineering, 21000 Novi Sad, Serbia*
[b]*University of Novi Sad, BioSense Institute, 21000 Novi Sad, Serbia. E-mail: nikola.kanas@gmail.com*
[c]*Texas A&M University, College Station, USA*
[d]*Serbian Academy of Sciences and Arts, 11000 Belgrade, Serbia*
[e]*University of Novi Sad, Faculty of Technical Sciences, 21000 Novi Sad, Serbia*

a result, pure MXenes terminated with specific gas-induced functional groups can be obtained using this method.[23] However, this method also requires a temperature above 500 °C and the use of highly toxic gases. In addition, it may face limitations in processing larger quantities of MXenes. Electrochemical etching is another alternative method proposed for synthesizing MXenes by selectively removing the A-layers from MAX phases. This approach utilizes a low-voltage electrochemical cell with a mild acidic electrolyte, typically diluted hydrochloric acid (HCl). While it offers a safer and more environmentally friendly alternative to conventional HF-based chemical etching, it also presents several challenges. These include the need for specialized electrochemical equipment and precise control over process parameters such as voltage and etching duration. Moreover, the incorporation of chlorine-containing surface terminations (–Cl) from the HCl electrolyte may alter the physicochemical properties of the resulting MXenes, potentially limiting their applicability in certain fields.[28,29]

While conventional top-down methods that involve MAX phase etching, a bottom-up synthesis method has also been reported.[30,31] For example, $Ti_2CCl_2$ was produced "atom by atom" by Chemical Vapor Deposition (CVD). This method enables the growth of MXene complex spherulite-like morphologies with no need for selective removal of "A" layers from MAX phase, and as such, represents a breakthrough in the MXene synthesis.[32] However, this method faces several challenges, including low production rates, limited control over morphology and crystallographic orientation, and the requirement for harsh processing conditions, which remain a key limitation of the CVD approach.[32]

To overcome the time-consuming nature and high energy consumption associated with conventional MXene synthesis *via* MAX phase etching, researchers have proposed microwave (MW)-assisted etching as an alternative approach.[33–50] This technique offers several advantages, including cost-effectiveness, operational convenience, improved controllability, rapid heating, and enhanced reaction kinetics. In this process, the selective removal of A-layer atoms from the MAX phase is significantly accelerated by the microwave heating effect. Although the energy of an individual MW photon (~0.0016 eV) is insufficient to directly break the chemical bonds within the MAX phase, microwave radiation can be efficiently absorbed by polar molecules such as HF and water due to their permanent dipole moments. This absorption induces molecular rotation, vibration, and friction, resulting in rapid localized dielectric heating within seconds, thereby promoting faster etching reactions.[51] Zhu *et al.* reported that after 15 min of microwave irradiation at a power of 200 W, temperatures exceeding 100 °C were achieved, which is sufficient to accelerate the etching process of the MAX phase.[52] Furthermore, during microwave synthesis, energy is generated within the medium itself rather than transferred from an external source, and combined with the high achieved temperatures, this results in a drastic reduction in synthesis time. During this process, hydrogen gas is rapidly generated, weakening the bonds between etched layers, aiding delamination. The reaction starts at the edges of the MAX phase, where etchant diffusion is most accessible, and progresses inward. As the A-layers are gradually removed, voids form and are swiftly filled by HF and water molecules, enabling further reactions on the planar surfaces.[42,53]

In conventional hydrothermal or chemical etching methods, the synthesis of MXenes typically involves prolonged reaction times (often hours or days), slow heat transfer through conduction and convection, and limited control over reaction selectivity and uniformity,[54,55] whereas the microwave etching process reduces the reaction time to minutes.[42] Beyond the obvious time efficiency, microwave-assisted etching offers enhanced reaction selectivity and improved yield, followed by sustainability goals – lowering energy input and minimizing environmental impact.[55,56] The shortest duration for successful microwave-assisted etching of MAX phases into MXenes, reported by Zhu *et al.*, was approximately 15 min.[52] Any further attempts to reduce this etching time resulted in the formation of multiphase products containing substantial amounts of unetched MAX phases.

In the present work, this etching time was further reduced to only 3 min of microwave exposure. This study highlights the practicality, convenience, and cost-effectiveness of microwave-assisted synthesis by employing a conventional microwave oven for MXene production. By applying a microwave power of 220 W for a total exposure time of 3 min, combined with intermediate mixing and cooling cycles, the fastest reported etching of $Ti_3AlC_2$ and $Ti_3AlCN$ MAX phases was achieved.

The implementation of 2D materials in sensing and biosensing platforms is a rapidly expanding field, yet developing affordable, high-performance systems remains a persistent challenge. The ability to pair a simplified, 3 min home-microwave synthesis with the exceptional properties of MXenes and their potential composites presents a compelling pathway for sensor innovation. Our method achieves a yield of 70% and higher, providing a substantial quantity of material for thorough investigative research. Furthermore, the rapid reaction time allows fresh batches to be produced on demand, ensuring a sustainable and efficient workflow. This study reports the initial electrochemical evaluation of the synthesized MXenes, establishing a foundation for their future integration into advanced sensing and biosensing applications.

## 2. Experimental details

### 2.1 Material synthesis

$Ti_3AlC_2$ MAX phase precursor was prepared by solid–state reaction synthesis, using Ti (Sigma-Aldrich, −100 mesh, 99.7%), Al (Alfa Aesar, −325 mesh, 99.5%), and TiC (Thermo Scientific, 99.5%) powders, mixed in a molar ratio of Ti/Al/TiC = 1.1 : 1.2 : 1.9. TiC is used as a precursor to prevent the excessive formation of intermediate phases and to simplify the overall reaction synthesis process, whereas 20% excess Al is used to compensate for the potential loss during high-temperature treatment, which could affect the stoichiometry of the desired MAX phase. To ensure homogeneity, the powders were ball-milled for 24 h using high-density zirconia ($ZrO_2$) beads at a rotation speed of 250 rpm. After ball milling, the powders were placed in alumina crucibles ($Al_2O_3$), and bulk $Ti_3AlC_2$ samples were synthesized in an inert argon (Ar) atmosphere using an MTI tube furnace

Table 1 Experimental details related to $Ti_3C_2$ and $Ti_3CN$ syntheses

| | | Etching cycle | | Mixing and cooling cycle | |
|---|---|---|---|---|---|
| MAX phase | MXene | Number of cycles | Duration of each MW cycle (min) | Number of cycles | Duration of each cycle (min) |
| $Ti_3AlC_2$ | $Ti_3C_2$ | 2 | 1.5 | 1 | 2 |
| $Ti_3AlCN$ | $Ti_3CN$ | 3 | 1 | 2 | 2 |

(Richmond, CA, USA) at 1510 °C with a dwell time of 4 h. Following synthesis, the bulk $Ti_3AlC_2$ was drill-milled, and the resulting powders were sieved to obtain a final particle size of less than 45 μm. On the other hand, $Ti_3AlCN$ powder (99%) with a particle size of about 35 μm was acquired from nanochemazone (Canada). Those MAX phase precursors were used for the synthesis of $Ti_3C_2$ and $Ti_3CN$ MXenes, by selective chemical etching of Al from the corresponding MAX phase in concentrated HF (48%). The MAX phase powders and concentrated HF acid were mixed in a 1 : 20 mass ratio (0.5 g MAX phase: 10 ml cc. HF) by gradually adding the MAX phase into the Teflon vessel with HF solution, over 2.5 min. After 5 min of magnetic stirring at room temperature, the stir bar was removed from the Teflon vessel, which was then placed in a MW oven (66, FUEGO, Spain) and subjected to short MW heating cycles of 1- or 1.5-minute-long MW exposure cycles at the power of 220 W. To enable efficient mixing and cooling, the Teflon vessel was transferred from the MW oven to the magnetic stirrer plate after each MW heating cycle, where it was stirred for 2 min after adding the stirring magnet to the vessel. This cycle costing of MW-assisted heating, stirring, and cooling was repeated 2–3 times, depending on the sample, as summarized in Table 1, whereas the schematics of the MAX phase etching and MXene production are shown in Fig. 1.

As noted in Table 1, the synthesis of $Ti_3CN$ was performed over more cycles than $Ti_3C_2$. Experimental results showed that $Ti_3CN$ tends to overheat more readily, due to the higher lattice energy of $Ti_3AlCN$ during microwave treatment. To manage this rapid energy release and preserve the structural integrity of the material, the synthesis was performed in multiple shorter cycles. After MW-assisted etching of both $Ti_3AlC_2$ and $Ti_3AlCN$ using the procedure described in Table 1, samples were water-washed out using a centrifuge (Centrifuge 5804, Eppendorf, USA) for 5 min at a speed of 4500 rpm. Supernatants were discarded after each centrifugation cycle until the pH reached a value of ~5.5. Once the supernatant turned dark – indicating the presence of dispersed MXene – it was collected and retained, while the etched sediment, herein referred to as the main sediment, was vacuum filtered and dried at 45 °C for 3 h in the vacuum oven (VSMD-30, Vims electric, India). The supernatant collected by washing was centrifuged once again at 7500 rpm, and the sediment collected after this step (herein referred to as the soft sediment) was also collected and dried using the same procedure as in the case of the main sediment. The final supernatant in this step was sonicated using an ultrasonic homogenizer (Sonopuls 70HD, Bandelin, Germany) at 70% power, employing continuous ultrasonic treatment for 30 min. A sample for electrochemical measurements was prepared by mixing 500 μl of MXene suspension and 500 μl of poly(3,4-ethylenedioxythiophene): polystyrene sulfonate PEDOT:PSS (Sigma-Aldrich, USA).

To calculate yields after MW-assisted etching, the mass of dried main sediments, dried soft sediments, and filtered MXenes from the final supernatants was measured and divided by the initial mass of MAX phase used for etching. MXenes were recovered from the final supernatant by vacuum filtration using a hydrophilic membrane filter with a pore size of 100 nm. The resulting films were dried in a vacuum oven at 45 °C for approximately 24 h before mass measurements.

### 2.2 Materials characterization

X-ray diffraction patterns (MiniFlex 600, Rigaku, Japan) of the MAX phase precursors, namely $Ti_3AlC_2$ and $Ti_3AlCN$, dried main sediments, were obtained by the diffractometer in the 5–60° $2\theta$ range in the range of 5–60° with a scanning rate of 0.11°/min to verify the phase purity of the synthesized materials. Flake size and morphological examination were performed using an Apreo 2C Scanning Electron Microscope (SEM, Thermo Fisher Scientific, Waltham, MA, USA), while the particle size and distribution were characterized using dynamic light scattering (Zetasizer, Malvern Instruments, UK), using the supernatant diluted in DI water to a concentration of approximately 0.01 mg $ml^{-1}$. The MXene surfaces were studied by X-ray photoelectron spectroscopy (XPS), using SPECS systems with XP50M X-ray source for Focus 500 and PHOIBOS100 energy analyzer using a monochromatized Al Kα X-ray source (1486.74 eV), operating at 12.5 kV and 250 W. Transmission electron microscopy (TEM) was conducted using a FEI Talos F200X microscope equipped with an X-FEG source and a maximum accelerating voltage of 200 kV, using both conventional and high-resolution transmission electron microscopy (TEM/HRTEM) mode and along with scanning transmission electron microscopy (STEM) mode drop casting diluted dispersion onto the carbon-coated copper grid. Atomic force microscopy (AFM) was performed by using the tapping mode in a Dimension Icon (Bruker) to evaluate the thickness of the particles in the MXene supernatant. To prepare a sample for AFM, a dilute (~0.01 mg $ml^{-1}$) dispersion of the final supernatant was dispersed in deionized (DI) water and drop-cast on a mica substrate, followed by drying in air before the analysis.

### 2.3 Electrochemical measurements

A commercial planar three-electrode carbon system (Metroohm DropSens DRP-C11L) was used, consisting of a working electrode coated with MXene/PEDOT: PSS composite, a carbon

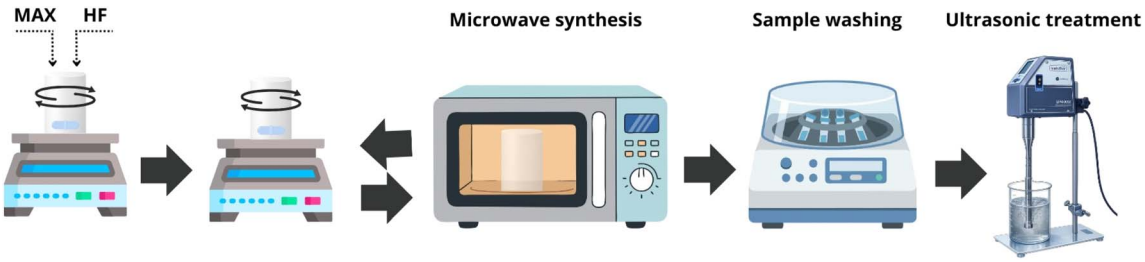


Fig. 1 Schematic illustration of the MAX phase etching and MXene delamination process.

counter electrode, an Ag/AgCl reference electrode, and potassium hexacyanoferrate (II, III) as a redox agent. Electrodes were cleaned in an ultrasonic methanol bath for 15 min to remove impurities before functionalization and electrochemical testing. Bare electrodes were first characterized with a redox probe using EIS and CV to establish baseline properties. Afterward, they were functionalized with an MXene/PEDOT:PSS composite to assess conductivity and performance. Since MXene flakes were unstable in aqueous suspension, PEDOT:PSS was used as a binding matrix; its positively charged PEDOT chains interact electrostatically with negatively charged MXene groups ($-O^-$, –OH, –F), while hydrogen bonding between –OH and –S further stabilizes the composite. The material was drop-cast onto electrodes, dried at 90 °C for 10 min, and stabilized overnight in a desiccator under an inert atmosphere. Measurements were performed with a PalmSens 4 Potentiostat/Galvanostat/Impedance Analyzer and PSTrace 5.8 software. CV was conducted between −0.8 and +0.8 V, and EIS from 1 Hz to 100 kHz with a 10 mV amplitude. The potential window was chosen to capture redox peaks without electrode degradation or side reactions. Impedance spectra were modeled with the open-source EIS Spectrum Analyzer using a Randles circuit (https://www.abc.chemistry.bsu.by/vi/analyser/).

## 3. Results and discussion

XRD patterns of $Ti_3AlC_2$ precursor, main sediment, and $Ti_3C_2$ nanosheets from supernatant are shown in Fig. 2a, while those for $Ti_3AlCN$ precursor, main sediment, and $Ti_3CN$ nanosheets from supernatant are shown in Fig. 2b. The diffraction patterns of precursors show a clear presence of sharp peaks corresponding to $Ti_3AlC_2$ and $Ti_3AlCN$. Small, minor peaks can be attributed to $Ti_2AlC$, $Ti_2AlCN$, and binary carbide $Ti_2CN$. More importantly, XRD results of $Ti_3C_2$ show a clear presence of strong intensity peaks, showing no presence of the MAX phase in the main sediment. On the other hand, $Ti_3CN$ sediment and even supernatant contain traces of MAX phase precursor, as observed in three reflection lines between 36° and 40° of 2$\theta$

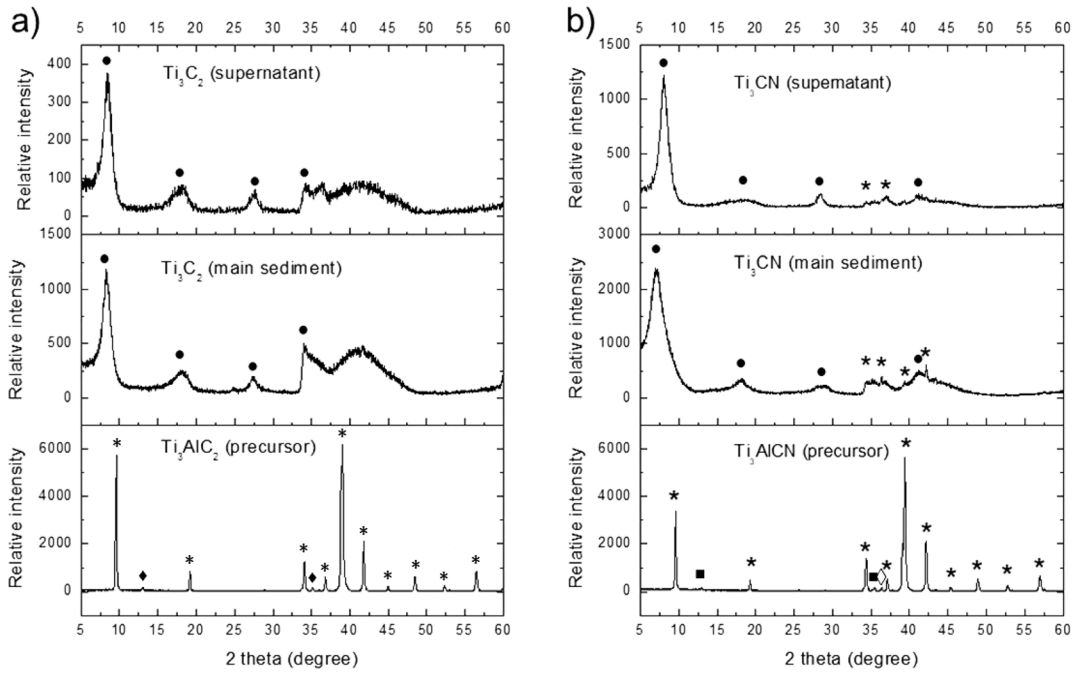


Fig. 2 X-ray diffraction patterns of the MAX phase precursors, the main sediment fractions, and the MXenes obtained from the final supernatants for (a) $Ti_3C_2$-based and (b) $Ti_3CN$-based samples. Diffraction peaks corresponding to pure MXene, $Ti_3AlC_2$ and $Ti_3AlCN$ MAX phaseses, $Ti_2AlC$, $Ti_2AlCN$, and $Ti_2CN$ are labeled with •,*, ◆, ■, and ◇, respectively. Peaks are indexed according to.[22,36,58]

Table 2 Crystallographic parameters of $Ti_3C_2$ and $Ti_3CN$ derived from X-ray diffraction patterns

| Material | *d*-spacing (Å) | FWHM (°) |
|---|---|---|
| $Ti_3C_2$ | 10.07 | 0.944 |
| $Ti_3CN$ | 11.26 | 1.2367 |

(Fig. 2b). Since $Ti_3CN$ is more resistant to etching compared to $Ti_3C_2$ due to stronger Ti–N bonds, leading to the slower or less noticeable formation of the accordion-like morphology.[57] It is worth noting that further optimization of the synthesis parameters could improve the purity of the obtained material. Extending the synthesis time represents one possible approach; however, fine-tuning and prolonging the mixing cycles may further contribute to achieving phase-pure MXenes, as this could improve the interfacial contact between the MAX phase and HF.

Furthermore, optimization of the centrifugation process might enable the complete removal of residual MAX phases from the system in cases where minor unetched remnants remain after synthesis, as observed in this work. The XRD pattern of $Ti_3C_2$ supernatant consists of phase-pure diffraction lines; therefore, used for electrochemical analysis. The interlayer spacing (*d*-spacing) calculated from the (002) diffraction peak was found to be 10.07 Å for $Ti_3C_2$ and 11.26 Å for $Ti_3CN$, indicating a more pronounced layer expansion in the latter (Table 2).

The *d*-spacing is slightly less than the most available in the literature, and it could be related to the fact that we do not intercalate Li+, nor any other cation. Furthermore, the presence of interlayered water molecules is limited due to the use of pure concentrated HF. Additionally, the kinetics of the MW etching are different from the conventional ones, so it is expected to reflect on the *d*-spacing too. It is important to note that the *d*-spacing value of for the synthesized $Ti_3C_2$ MXene reflects the material in its bulk, powder form. However, prior to electrochemical characterization and electrode preparation, the MXene suspension undergoes sonication. This process is specifically intended to promote the separation of the 2D layers and enhance the accessibility of active sites.

Since there was almost no waste due to efficient etching, except for that during washing, it was quite expected to obtain high yields. The yields ($y$) were calculated using eqn (1):

$$y = (m_{(\mathrm{MXene})}/m_{(\mathrm{MAX\ phase})}) \cdot 100 \quad (1)$$

where $m_{(\mathrm{MXene})}$ represents the weight of produced dried MXene flakes, including sediments, and final supernatants, and $m_{(\mathrm{MAX\ phase})}$ represents the weight of pre-etched, washed MAX phase. Table 3 contains an overview of the mass changes at each step in the synthesis process, including the final yields that are about 90% and 70% for $Ti_3C_2$ and $Ti_3CN$, respectively.

As noted by Chen *et al.*, the substitution of carbon with nitrogen increases the Young's modulus of the $Ti_3AlCN$ MAX phase by approximately 20 GPa, significantly enhancing its mechanical and chemical stability.[59] Nevertheless, the formation of intermediate phases and impurities (such as TiN, TiC, $Ti_2AlN$ and $Ti_2AlC$) is commonly associated with the complex reaction kinetics of quaternary MAX phases.[59] These properties explain the lower yield of $Ti_3CN$ compared to $Ti_3C_2$.

SEM images of the as-etched main sediment with an accordion-like structure are displayed in Fig. 3a. The spacing between the plates is pronounced due to an enormous amount of $H_2$ gas that is rapidly released during a very short reaction time. However, the $Ti_3C_2$ structure (Fig. 3a) is more open than the $Ti_3CN$ ones (Fig. 3b), and as such, probably results in better delamination and a higher amount of produced material (Table 3). The synthesis time of 3 min is the minimum required for obtaining a phase-pure $Ti_3CN$, too, and some extension in synthesis time might result in a more open accordion-like structure and therefore, could result in even higher yields. Fig. 3c and d give insights into a flake-like morphology of the soft sediments, with the flake size over a micron for both $Ti_3C_2$ and $Ti_3CN$. However, due to invasive delamination by probe sonication, the supernatant flakes are reduced in size to a submicron level (Fig. 3e and f). Such a destructive method of delamination significantly increases the yield. In most cases, reducing the size of MXene flakes is undesirable, especially when high electrical conductivity is required.[37,38] On the other hand, for electrochemical applications, size reduction makes a positive impact.

AFM analysis of the dispersed $Ti_3C_2$ MXene from the supernatant was conducted to elaborate the flake thicknesses and thus, to evaluate the delamination process. According to the variations in height profiles (Fig. 4), many flakes are found to be in the form of 2–3 stacked layers (4–6 nm), rather than monolayers with the expected range 1.5–1.8 nm.

Flake delamination after etching done by concentrated HF requires the use of TBAOH or TMAOH intercalates, or mechanical exfoliation methods such as probe sonication.[60] The present results indicate that delamination by probe sonication was successfully performed; however, complete delamination, including a predominance of monolayers, was not fully achieved, likely due to insufficient sonication power or exposure time. Fig. 5 provides additional evidence of a $Ti_3C_2$ and $Ti_3CN$ flake size and distribution, expressed *via* volume percentage. Considering the distribution given in both expressions, the

Table 3 Overview of the mass changes for each step in the synthesis process, including the final yields

| Material | MAX phase (mg) | Main sediment (mg) | Soft sediment (mg) | Supernatant (mg) | Yield (%) |
|---|---|---|---|---|---|
| $Ti_3C_2$ | 500 | 320.65 | 92.34 | 36.37 | 89.9 |
| $Ti_3CN$ | 500 | 259.34 | 63.57 | 28.48 | 70.3 |

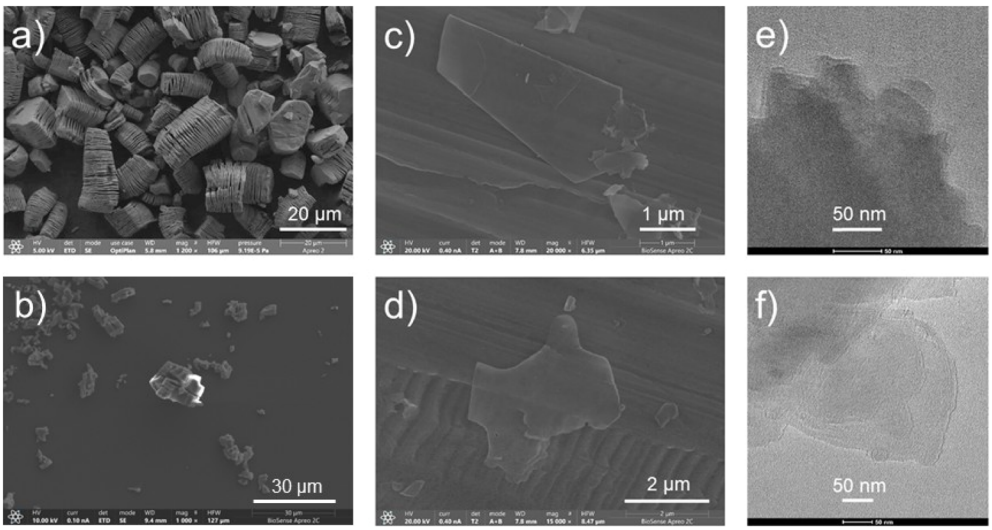


Fig. 3 SEM images of: (a) main sediment of $Ti_3C_2$; (b) main sediment of $Ti_3CN$; (c) soft sediment of $Ti_3C_2$; (d) soft sediment of $Ti_3CN$; and TEM images of: (e) supernatant $Ti_3C_2$; (f) supernatant $Ti_3CN$.

flakes are not so uniform in size, whereas the most dominant flakes are with a size of about 400 nm. It is good to point out that the DLS method is not so accurate for particles with a plate-like morphology due to a "spherical" approximation, being even more pronounced when the flakes are shift-stacked. Also, it must be emphasized that the maximum measuring range of the apparatus is 1000 nm, and therefore, larger flakes were not evidenced.

Fig. 6 and 7 show XPS spectra of the C 1s, Ti 2p, and O 1s core levels for $Ti_3C_2$ and $Ti_3CN$, respectively. F 1s core levels are given in Fig. S3. The binding energy of C 1s for both MXenes is positioned at about 282 eV, which means that the binding energy of C atoms in the octahedral sides (Ti–C–Ti) is not affected by surface terminations of HF, as well as the presence of an N atom at the X position.[39,40] So, besides the C 1s core level (Fig. 6), there is one from C–C contaminations at around 285.1 eV, and two originating from C–O and O–C–O contaminations at 286.4 and 289.0 eV, respectively. The relative intensities of these peaks can be used to assess the degree of surface functionalization *versus* contamination. The Ti 2p region is insufficiently informative for understanding the oxidation state of titanium in $Ti_3C_2$.

The Ti 2p peaks consist of spin–orbit splitting (doublets), whereas the spectra are usually split into Ti $2p_{3/2}$ and Ti $2p_{1/2}$, and the ratios slightly deviate from the expected due to the Coster-Kronig effect.[39,40] Here we used Tougaard background since it has been shown to give better quantitative results, and the doublets shown in Fig. 7 Ti 2p originate from Ti–C, Ti–O, and Ti–F. Similar correlations could be found with $Ti_3CN$, too (Fig. 7). The components with the highest binding energies (~458.0–459.5 eV) are attributed to $Ti^{4+}$ species resembling $TiO_2$, indicating partial oxidation of titanium atoms, likely resulting from surface hydroxylation or ambient air exposure. The coexistence of $Ti^{3+}$ and $Ti^{4+}$ oxidation states suggests that the $Ti_3C_2T_x$ surface is not exclusively composed of Ti–C bonds, but also includes oxidized titanium species, which may

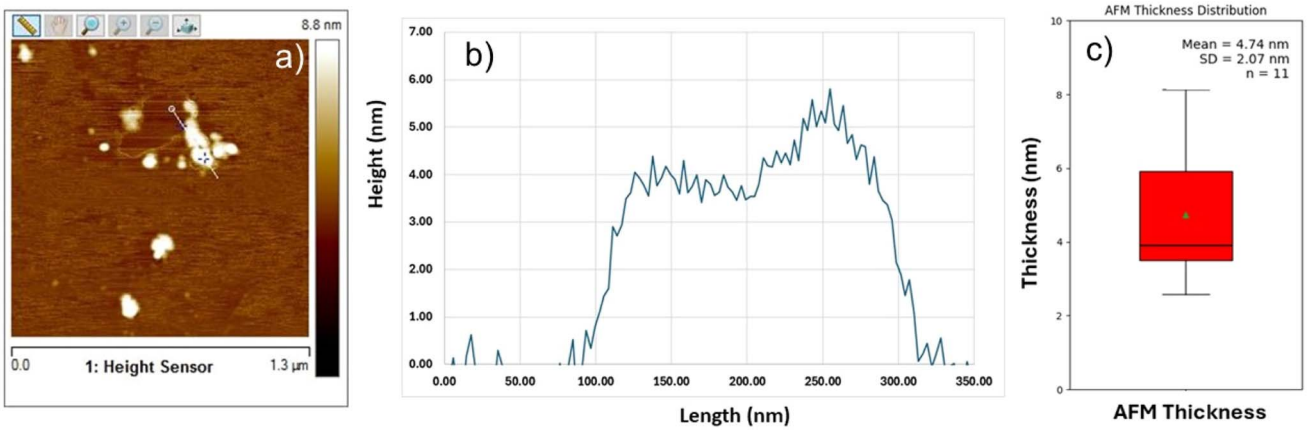


Fig. 4 (a) atomic force microscope (AFM) image of $Ti_3C_2$ flake with (b) corresponding variations in height profiles as a function of its length, (c) statistical distributions of AFM thickness.

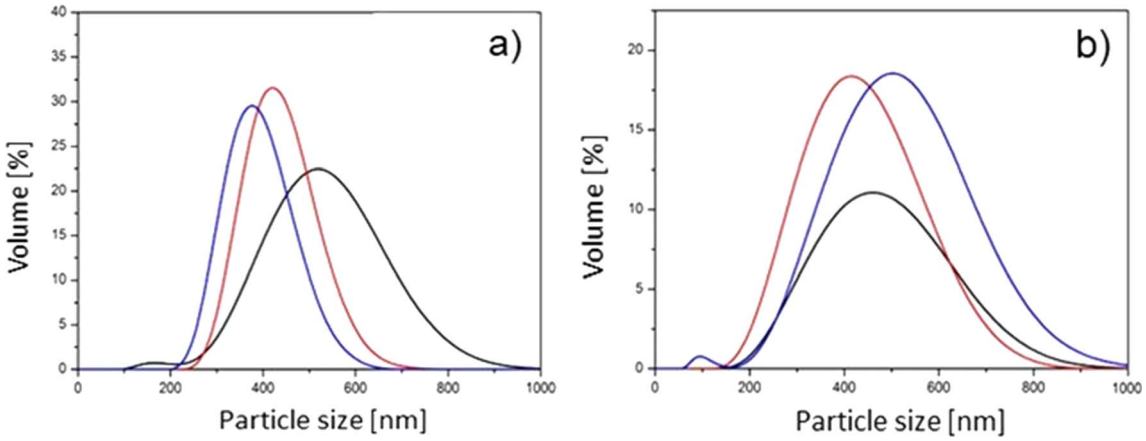


Fig. 5 DLS analysis of (a) $Ti_3C_2$ and (b) $Ti_3CN$ flakes.

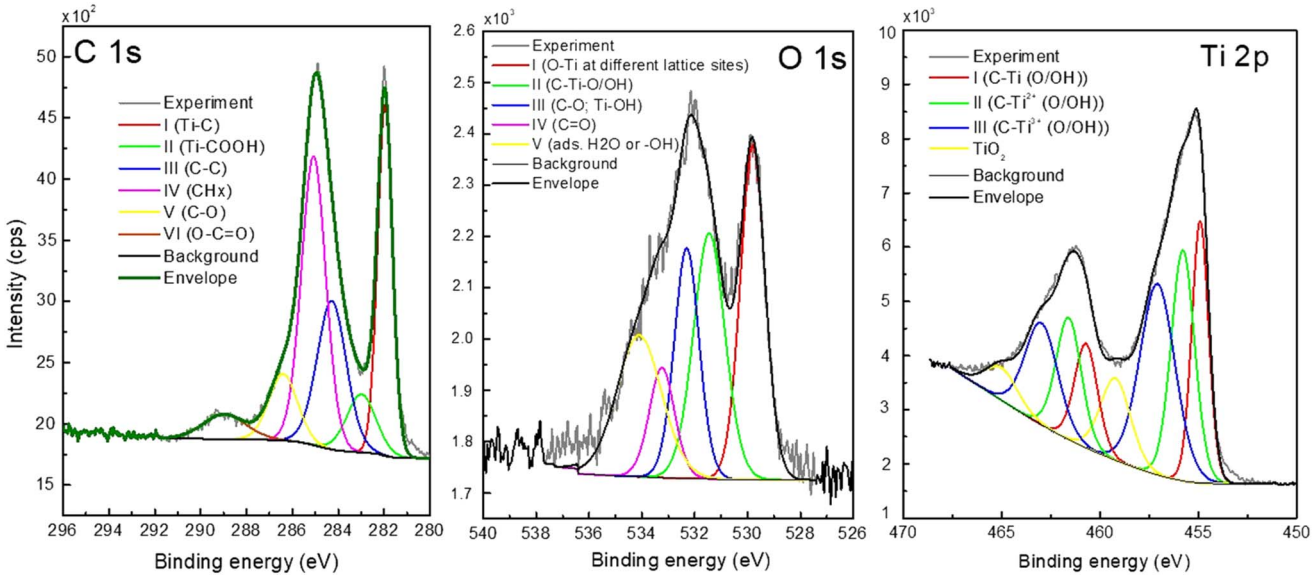


Fig. 6 XPS analysis of $Ti_3C_2$.

significantly affect its electrochemical and catalytic behavior. More detailed explanations and an in-depth understanding are reported by Natu *et. al.*[61]

Cyclic Voltammetry (CV) and Electrochemical Impedance Spectroscopy (EIS) were employed to assess the electrochemical performance of synthesized MXenes (Fig. 8). CV analysis provided insights into the redox activity and catalytic behavior of the modified electrodes by observing oxidation and reduction peak intensities. Oxidation occurs at the working electrode as analytes donate electrons, while reduction takes place during the reverse scan. The high surface area and conductivity of MXenes enhance redox responses and overall sensor efficiency.

EIS was used to analyze processes at the electrode/electrolyte interface using equivalent Randles circuits (Fig. S2). The bare and PEDOT:PSS-modified electrodes followed the model from Fig. S2a, while the MXene/PEDOT:PSS composite required additional elements (Fig. S2b) to account for its interfacial complexity. CV results (Fig. 8a) showed increased current and linear ionic and cationic peaks intensity dependence on the square root of scan rate. MXene/PEDOT:PSS composite revealed a linear relationship (Fig. 8a), with a slope of 2.31 mA ($mV^{-1}$ $s)^{1/2}$ and a high correlation coefficient ($R^2 = 0.995$).

This confirms that the electrochemical reaction is predominantly diffusion-controlled. The increase in current observed in CV measurements upon addition of a new material to the electrode indicates enhanced electrochemical activity, Fig. 8d, as a result of improved electron transfer kinetics and increased electroactive surface area. The composite material demonstrated a ~46% enhancement in current response compared to pure PEDOT:PSS. At 0.4 V, the current was 1082 mA for the MXene/PEDOT:PSS composite, substantially higher than the 741 mA measured for PEDOT:PSS alone. Stability tests (Fig. 8c) demonstrated consistent redox peaks after 25 scans, highlighting the good electrochemical stability of the composite.

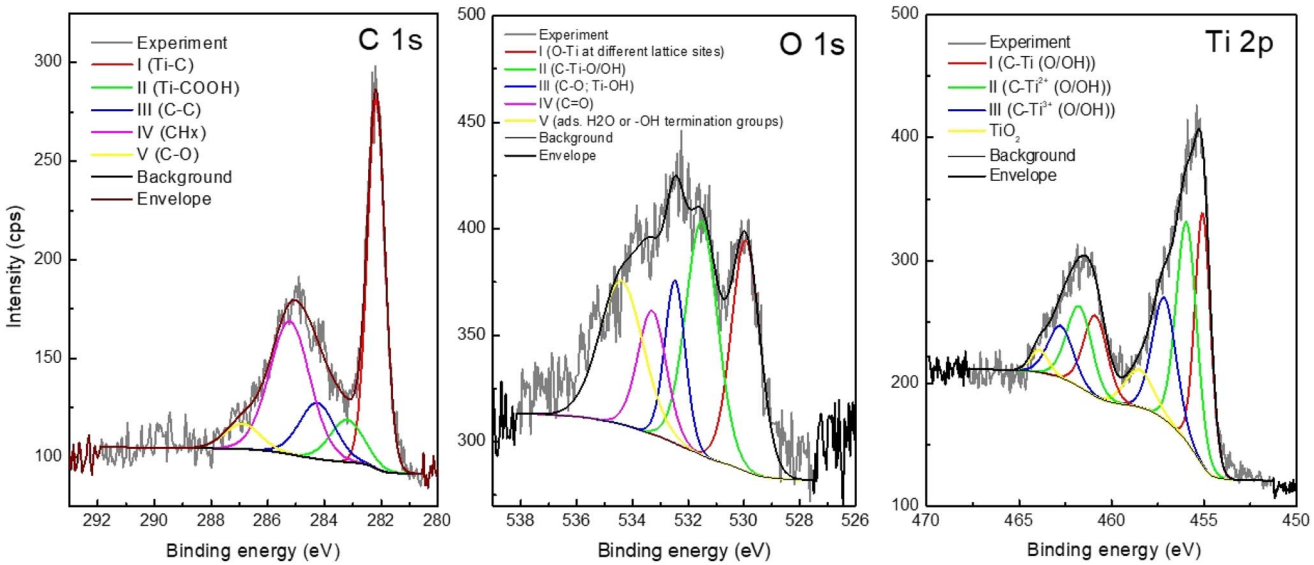


Fig. 7 XPS analysis of $Ti_3CN$.

In the literature, MXene is most commonly used for sensors and energy storage applications due to its capacitive properties. When examined as a capacitor, cyclic voltammetry (CV) is often conducted to evaluate its stability. For instance, in the study by Mahmood *et al.*,[62] MXene was used in a composite with manganese oxide and demonstrated excellent stability. In line with these findings, the electrochemical results presented in this work indicate good stability of the MXene/PEDOT:PSS composite with the provided 25 CV scans, along with favorable conductivity and reversibility of electrochemical reactions. These results offer concrete insights into the potential of the composite material for application in electrochemical biosensors or gas sensors. Moreover, the synthesis approach applies not only to Ti-based MXenes but also to other types and a wider range of applications, including biomedical ones.

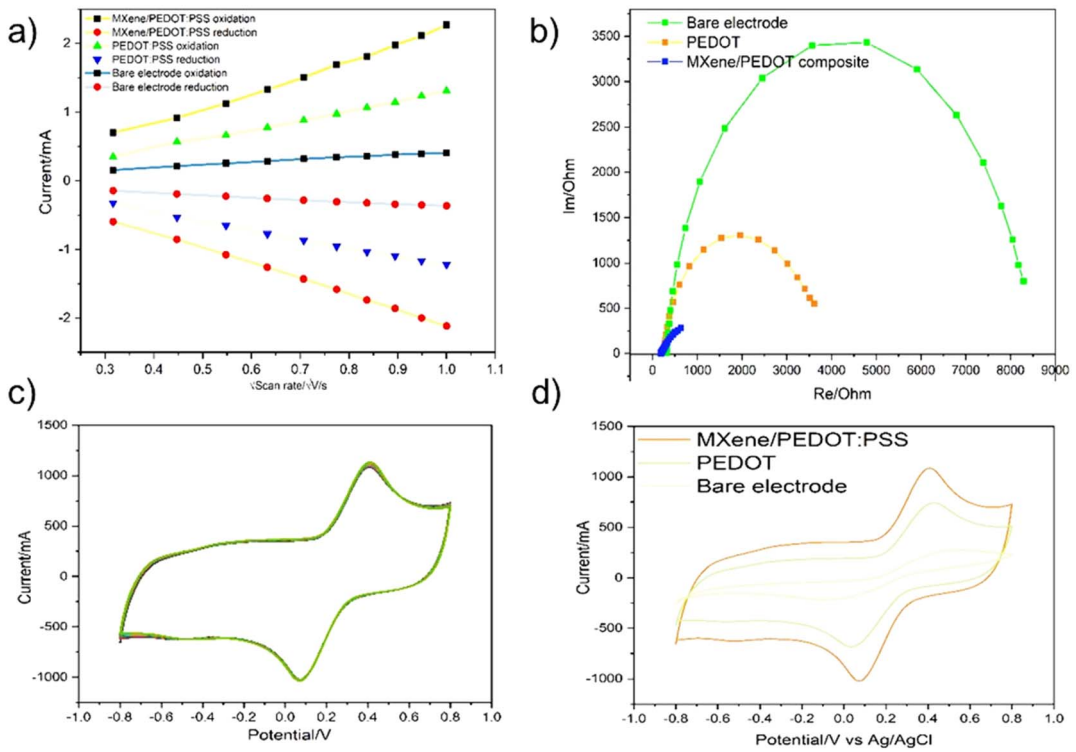


Fig. 8 (a) The dependence of anionic and cationic peak intensity on the square root of scan rate of bare electrode, PEDOT: PSS and $Ti_3C_2$/PEDOT: PSS composite; (b) EIS measurements with bare electrode, PEDOT: PSS and $Ti_3C_2$/PEDOT: PSS composite; (c) stability test of the composite by 25 scans (d) CV of $Ti_3C_2$/PEDOT: PSS composite, PEDOT: PSS and bare electrode.

An electrostatically stable $Ti_3C_2$/PEDOT: PSS composite demonstrates excellent film-forming ability, flexibility, and stability, as well as good electrochemical properties. By combining them, we improved the overall conductivity, mechanical integrity, and electrochemical performance of the sensing layer, facilitating better electron transfer and more stable signal output. These results offer concrete insights into the potential of the composite material for application in electrochemical biosensors or gas sensors.

## 4. Conclusions

Here we report on the fastest-ever obtained synthesis of $Ti_3C_2$ and $Ti_3CN$. A complete etching of $Ti_3AlC_2$ and $Ti_3AlCN$ was achieved after only 3 min of microwave irradiation in concentrated HF, resulting in 90% and 70% yields, respectively. The obtained etching sediments (main sediments) were MXene-pure with negligible traces of MAX phase precursors. Delamination was performed solely by probe sonication (without intercalation), producing flakes composed of 2–3 stacked monolayers, accompanied by a notable reduction in flake size. Surface terminations were characteristic of HF-based etching, consisting of –F, –OH, and –O groups. The resulting $Ti_3C_2$/PEDOT:PSS composites exhibited stable redox behavior, as indicated by consistent redox peak responses over multiple cycles, thereby underscoring their potential for electrochemical sensing applications.

In addition to great structural and electrochemical properties, this synthesis route is also economically advantageous due to its significantly reduced processing time. Although this approach successfully yielded two MXenes with record-fast etching times, further research should focus on optimizing synthesis parameters for a broader range of MXene compositions, as well as on exploring alternative, safer etching reagents. In particular, minimizing or eliminating the use of hydrofluoric acid (HF) remains an important objective, as HF is highly corrosive and hazardous, requiring specialized laboratory infrastructure, including PTFE-compatible work surfaces, fume hoods, HF-resistant laboratory consumables, and strict safety protocols for handling and disposal.

## Conflicts of interest

There are no conflicts to declare.

## Data availability

The data supporting the findings of this study are available on the Zenodo platform. Additional materials can be obtained from the corresponding author upon reasonable request.

Supplementary information (SI): X-ray diffractograms of $Ti_3C_2$ and $Ti_3CN$ etched for varying times, indicating why specific etching durations were chosen, diffusion-controlled impedance analysis of the MXene/PEDOT:PSS composite. See DOI: https://doi.org/10.1039/d5ra10068b.

## Acknowledgements

This work was funded by the European Union under the ANTARES project, which received funding from the Horizon 2020 research and innovation program under GA. No. 739570 and under the Know4Nano project, which receives funding for the Horizon Europe project under GA. No. 101159710, and by the LABOUR project (6710), the Science Fund of the Republic of Serbia. MSc. Marko Radenković, MSc. Elvira Toth, Dr Frode H. Fagerli, and Prof. Miladin Radović are acknowledged by JP and NK. for the technical support and fruitful discussions. We also acknowledge the financial support provided by the Serbian Academy of Science and Arts, Project F-137. M. Dujovic is grateful to the U.S. National Science Foundation for supporting their work on MXenes (award # 2240554).

## References

1 M. Naguib, M. Kurtoglu, V. Presser, J. Lu, J. Niu, M. Heon, L. Hultman, Y. Gogotsi and M. W. Barsoum, *Adv. Mater.*, 2011, **23**, 4248–4253.
2 Y. Gogotsi and B. Anasori, *ACS Nano*, 2019, **13**, 8491–8494.
3 B. Anasori and Y. Gogotsi, *Graphene 2D Mater.*, 2022, **7**, 75–79.
4 D. Li, W. Zheng, S. M. Gali, K. Sobczak, M. Horák, J. Polčák, K. Dziubaniuk, R. Kubíček, A. Pleštilová, P. Kulhánek, T. Patočka, J. Přech, L. Palatinus, M. Kalbáč, J. Václavík and X. Feng, *Nat. Mater.*, 2024, **23**, 1085–1092.
5 V. Kotasthane, D. Holta, X. Zhao, J. Lutkenhaus, M. Green and M. Radovic, *J. Mater. Res.*, 2023, **38**, 1527–1542, DOI: 10.1557/s43578-023-00915-z.
6 V. Natu, R. Pai, M. Sokol, M. Carey, V. Kalra and M. W. Barsoum, *Chem*, 2020, **6**, 616–630.
7 J. Yoon, M. Shin, T. Lee and J.-W. Choi, *Materials*, 2020, **13**, 299, DOI: 10.3390/ma13020299.
8 M. Sadiq, Q. N. K. Hoang, A. Kishlock, F. G. Sabzevari, K. Katti, D. Katti, Q. Zhang and D. Wang, *Cancer Plus*, 2024, **6**, 3793, DOI: 10.36922/cp.3793.
9 D. Qin, C. Liu, K. Song and S. Ramakrishna, *Chem. Eng. J.*, 2025, **525**, 170300, DOI: 10.1016/j.cej.2025.170300.
10 N. T. Padmanabhan, K. Gayathri, R. M. Thomas and H. John, *Energy Environ. Sustainability*, 2025, **1**(3), 100042.
11 J. Zhang, Y. Zhao, X. Guo, C. Chen, C.-L. Dong, R.-S. Liu, C.-P. Han, Y. Li, Y. Gogotsi and G. Wang, in *MXenes*, Jenny Stanford Publishing, 2023.
12 B. Anasori, M. R. Lukatskaya and Y. Gogotsi, *Nat. Rev. Mater.*, 2017, **2**, 16098, DOI: 10.1038/natrevmats.2016.98.
13 F. Shahzad, M. Alhabeb, C. B. Hatter, B. Anasori, S. Man Hong, C. M. Koo and Y. Gogotsi, *Science*, 2016, **353**, 1137–1140.
14 D. Sun, M. Wang, Z. Li, G. Fan, L.-Z. Fan and A. Zhou, *Electrochem. Commun.*, 2014, **47**, 80–83.
15 F. Meng, M. Seredych, C. Chen, V. Gura, S. Mikhalovsky, S. Sandeman, G. Ingavle, T. Ozulumba, L. Miao, B. Anasori and Y. Gogotsi, *ACS Nano*, 2018, **12**, 10518–10528.
16 A. Alikhanian, M. N. Montazer, B. Ahmadi, M. Mahdavi, N. Sadeghian, G. Tüzün, B. Tuzun, P. Taslimi and K. Sayın,

in *MXenes as Surface-Active Advanced Materials*, ed. M. A. Quraishi, C. Verma and E. Berdimurodov, Elsevier, 2024, 437–456.
17 G. Deysher, C. E. Shuck, K. Hantanasirisakul, N. C. Frey, A. C. Foucher, K. Maleski, A. Sarycheva, V. B. Shenoy, E. A. Stach, B. Anasori and Y. Gogotsi, *ACS Nano*, 2020, **14**, 204–217.
18 A. VahidMohammadi, J. Rosen and Y. Gogotsi, *Science*, 2021, **372**, eabf1581.
19 Z. Jiang, Z. Pang, S. Chen, F. Tian, X. Zhang, F. Wang, X. Xia, C. Chen, G. Li, Q. Xu, X. Lu and X. Zou, *JOM*, 2025, **77**, 697–706.
20 K. Arole, J. W. Blivin, S. Saha, D. E. Holta, X. Zhao, A. Sarmah, H. Cao, M. Radovic, J. L. Lutkenhaus and M. J. Green, *iScience*, 2021, **24**, 103403.
21 Z. Guo, X. Xu, L. Liu, C. Wang, Z. Li, W. Shi, Z. Zhang and M. Li, *Adv. Energy Mater.*, 2023, **13**, 2300890, DOI: 10.1002/aenm.202300890.
22 K. Arole, J. W. Blivin, A. M. Bruce, S. Athavale, I. J. Echols, H. Cao, Z. Tan, M. Radovic, J. L. Lutkenhaus and M. J. Green, *Chem. Commun.*, 2022, **58**, 10202–10205.
23 J. Zhu, S. Zhu, Z. Cui, Z. Li, S. Wu, W. Xu, B. Te, Y. Liang and H. Jiang, *Energy Storage Mater.*, 2024, **70**, 103503.
24 Z. Lei, Y. Zhang, X. Wang, L. Wang, M. Luo, X. Zhao and Z. Guo, *ACS Omega*, 2024, **9**, 44849–44872, DOI: 10.1021/acsomega.4c04849.
25 Y. Guo, S. Jin, L. Wang, P. He, Q. Hu, L.-Z. Fan and A. Zhou, *Ceram. Int.*, 2020, **46**, 19550–19556.
26 T. T. Mashangva, A. Goel, U. Bagri, S. Prasher, A. Sharma and M. K. Singh, *Appl. Mater. Today*, 2024, **30**, 102163, DOI: 10.1016/j.apmt.2024.102163.
27 T. T. Mashangva, N. Vishwakarma, P. P. Singh, S. Prasher, R. Dhiman, M. Kumar and A. Sharma, *J. Energy Storage*, 2026, **150**, 120387, DOI: 10.1016/j.est.2026.120387.
28 W. Sun, S. A. Shah, Y. Chen, Z. Tan, H. Gao, T. Habib, M. Radovic and M. J. Green, *J. Mater. Chem. A*, 2017, **5**, 21663–21668.
29 A. Thakur, A. Sarycheva, A. Ouisse, J. E. Halim and B. Anasori, *Small Methods*, 2023, **7**, 2300030, DOI: 10.1002/smtd.202300030.
30 A. K. Singh, S. Shukla, P. K. Rout, V. S. Vemuri and C. S. Rout, *Chem. – Eur. J.*, 2020, **26**, 17547–17559.
31 A. Rasool, S. Kanwal, M. Umer, A. Rasheed, M. N. Tahir and M. Sher, *Biomed. Eng.*, 2021, **20**, 73.
32 D. Wang, C. Zhou, A. S. Filatov, W. Cho, F. Lagunas, M. Wang, S. Vaikuntanathan, C. Liu, R. F. Klie and D. V. Talapin, *Science*, 2023, **379**, 1242–1247.
33 H. Zaharin, M. Ghazali, A. Numan, M. Khalid, T. Nagarajan, F. Ezzah and A. Rasheed, *Lubricants*, 2023, 775–782.
34 Q. Wu, Y. Ren, P. Li, Y. Wang, Z. Yang, K. Qu, G. Qi, S. Chen and F.-F. Wu, *Appl. Phys. A*, 2021, **127**, 360, DOI: 10.1007/s00339-021-04530-9.
35 Q. Wu, Y. Wang, P. Li, S. Chen and F. Wu, *Appl. Phys. A*, 2021, **127**, 822.
36 M. Liu, Y. Bai, Y. He, J. Zhou, Y. Ge, J. Zhou and G. Song, *Mikrochim. Acta*, 2021, **188**, 15.
37 F. N. M. Azlan, M. A. A. M. Abdah, Y. S. Tan, M. N. Mustafa, R. Walvekar and M. Khalid, *J. Energy Storage*, 2023, **72**, 108620, DOI: 10.1016/j.est.2023.108620.
38 Y. Zhong, Y. Li, M. Wu, J. Yang, J. Liu, X. Liu, Z. Li and Y. Gogotsi, *Adv. Sci.*, 2024, **11**, 2405686, DOI: 10.1002/advs.202405686.
39 M. A. A. M. Abdah, J. Cherusseri, N. A. Dzulkarnain, M. Mokhtar, M. S. Su'ait, Y. S. Tan, M. N. Mustafa, M. Khalid, A. Numan and A. Radwan, *J. Electroanal. Chem.*, 2023, **928**, 117050.
40 K. Mahabari, R. D. Mohili, M. Patel, A. H. Jadhav, K. Lee and N. K. Chaudhari, *Nanoscale Adv.*, 2024, **6**, 5388–5397, DOI: 10.1039/d4na00250d.
41 X. Zhang, Y. Liu and J. Zhang, *Adv. Energy Mater.*, 2023, **13**, 2200890.
42 A. Numan, S. Rafique, M. Khalid, H. A. Zaharin, A. Radwan, N. A. Mokri, O. P. Ching and R. Walvekar, *Mater. Chem. Phys.*, 2022, **288**, 126429.
43 C. Xie, L. Xu, J. Peng and L. Zhang, *Adv. Funct. Mater.*, 2023, **32**, 2201378.
44 T. T. Mashangva, N. Vishwakarma, S. Prasher, A. Sharma, M. Shrivastav, R. Dhiman and M. Kumar, *Chem. Eng. Commun.*, 2026, **213**(2), 346–364, DOI: 10.1080/00986445.2025.2549910.
45 U. Bagri, A. Thakur, A. Sharma, D.-V. N. Vo and P. P. Singh, *Int. J. Environ. Anal. Chem.*, 2025, 1–25.
46 U. Bagri, S. Jan, A. Sharma and P. P. Singh, *Top. Catal.*, 2025, **15**, 26240, DOI: 10.1038/s41598-025-26240-5.
47 J. Yang Lu, Z. Qi Bu, Y. Qing Lei, D. Wang, B. He, J. Wang and W. T. Huang, *J. Mol. Liq.*, 2024, **409**, 125503, DOI: 10.1016/j.molliq.2024.125503.
48 P. E. Lokhande, P. Misal, R. S. Kalubarme, M. V. Kulkarni, U. Rednam, S. Padlkar and B. A. Al-Asbahi, *Diamond Relat. Mater.*, 2025, **157**, 112503, DOI: 10.1016/j.diamond.2025.112503.
49 P. E. Lokhande, U. Rednam, V. Kadam, C. Jagtap, D. Kumar and R. Aepuru, *Chem. Commun.*, 2025, **61**, 2111–2114, DOI: 10.1039/d4cc04765f.
50 P. E. Lokhande, U. Rednam, V. Kadam, C. Jagtap, S. R. Padalkar, R. Bhat, T. Boobalan and B. A. Al-Asbahi, *New J. Chem.*, 2025, **49**, 4248–4255, DOI: 10.1039/d5nj00142k.
51 J. P. Tierney and P. Lidström, *Microwave Assisted Organic Synthesis*, 2009.
52 J. Zhu, J. Zhang, R. Lin, B. Fu, C. Song, W. Shang, P. Tao and T. Deng, *Chem. Commun.*, 2021, **57**, 12611–12614, DOI: 10.1039/d1cc04989e.
53 F. E. Ab Latif, M. Khalid, A. Numan, N. Abdul Manaf, N. Mujawar Mubarak, H. A. Zaharin and E. Chan Abdullah, *J. Mol. Struct.*, 2025, **1329**, 141407, DOI: 10.1016/j.molstruc.2025.141407.
54 F. B. (Bibi), S. Ee Lam, M. Khalid and J. Arshid Numan, *Solid State Sci. Technol.*, 2025, **14**, 1005, DOI: 10.1149/XXX.
55 A. J. Khan, L. Gao, A. Numan, S. Khan, I. Hussain, M. Sajjad, S. S. Shah, A. Mateen and G. Zhao, *Crit. Rev. Solid State Mater. Sci.*, 2025, **50**, 515–538, DOI: 10.1080/10408436.2024.2446049.

56 F. E. Ab Latif, A. Numan, N. M. Mubarak, M. Khalid, M. A. A. M. Abdah and W. P. Wong, *Mater. Today Sustain.*, 2024, **28**, 100996, DOI: 10.1016/j.mtsust.2024.100996.
57 W. Zhang, S. Li, X. Fan, X. Zhang, S. Fan and G.-P. Bei, *Carbon Energy*, 2024, **6**, 717, DOI: 10.1002/cey2.609.
58 T. S. Mathis, K. Maleski, A. Goad, A. Sarycheva, M. Anayee, A. C. Foucher, K. Hantanasirisakul, C. E. Shuck, E. A. Stach and Y. Gogotsi, *ACS Nano*, 2021, **15**, 6420–6429, DOI: 10.1021/acsnano.0c08357.
59 N. Chen, H. Huang, Z. Xu, Y. Xie, D. Xiong, X. Chu, B. Gu, B. Zheng, W. Deng, H. Zhang and W. Yang, *Chin. Chem. Lett.*, 2020, **31**, 1044–1048, DOI: 10.1016/j.cclet.2019.10.004.
60 A. VahidMohammadi, E. Kayali, J. Orangi and M. Beidaghi, Techniques for MXene Delamination into Single-Layer Flakes, in *2D Metal Carbides and Nitrides (MXenes)*, ed. B. Anasori and Y. Gogotsi, Springer, 2019, pp. 177–195.
61 V. Natu, M. Benchakar, C. Canaff, A. Habrioux, S. Célérier and M. W. Barsoum, *Matter*, 2021, **4**, 1224–1251, DOI: 10.1016/j.matt.2021.01.015.
62 M. Mahmood, A. Rasheed, I. Ayman, T. Rasheed, S. Munir, S. Ajmal, P. O. Agboola, M. F. Warsi and M. Shahid, *Energy Fuels*, 2021, **35**, 3469–3478.